42nd AIAA/ASME/SAE/ASEE Joint Propulsion Conference & Exhibit
9 - 12 July 2006, Sacramento, California

AIAA 2006-4743

LES of Premixed Combustion in the Stagnation Point Reverse Flow Combustor

S. Undapalli*
S. Menon†
School of Aerospace Engineering
Georgia Institute of Technology
Atlanta, Georgia 30332

Abstract

A lab-scale burner, referred to as the Stagnation Point Reverse Flow (SPRF) combustor has been built at Georgia Tech, which incorporates a novel design to achieve exhaust-gas recirculation, premixing, and dilution. This combustor has shown the potential to meet the conflicting requirements of low pollution and high efficiency. Large Eddy Simulations (LES) are used to characterize the flow field and combustion phenomenon for the premixed mode of operation. The computed mean and root mean square (RMS) quantities agrees well with the measurements. All the observed features such as the enhanced entrainment and mixing of the returning hot products into the incoming reacting jet are resolved in the computations. The primary stabilization zone in the SPRF combustor, which is considered to be the region of low mean and high fluctuating velocities is also captured in the computations. Karlovitz numbers are evaluated and the combustion phenomenon in SPRF combustor is found to operate in thin flame regions. The potential of SPRF combustor to produce low NO is also demonstrated by LES using global NO mechanisms.

I. Introduction

The demand for low emissions along with more energy efficiency has been a major driving force to develop innovative combustion technologies. Internal preheating, lean premixed combustion and exhaust gas recirculation are among the most popular techniques to obtain this goal. Including these effects have shown that the flame structure is strongly related to the mixing patterns in the entire combustor,[1] and also resulted in low NOx.[2]

A compact, low emissions combustor design that incorporates the above mentioned techniques has recently been demonstrated,[3] and is referred to as Stagnation Point Reverse Flow (SPRF) combustor. SPRF incorporates a novel design to achieve exhaust-gas recirculation, premixing and dilution, and also allows it to operate in premixed or non-premixed mode with a great flexibility to vary parameters at ease. Unlike most combustors, the reactants and products enter and leave at the same end. The schematic sketch is shown in Fig. 1. The experimental apparatus consist of three main components: a combustor, an injector and an air/fuel supply system. The combustor is a cylindrical quartz tube (4) wrapped with thermal insulation, and closed on one side with an end plate (6) (stagnation end). The injector is located at the open end of the tube (opposite to the end plate) with its axis coinciding with the axis of the cylindrical quartz tube. The injector consists of concentric tubes to discharge the fresh mixture into the combustor. An unique feature of SPRF is that no swirl or bluff body is needed to stabilize the flame and this has some obvious structural design advantages. In the non-premixed mode, fuel flows through the central tube (2) and the air flows through the concentric annular tube (3) surrounding

*Graduate Research Assistant, AIAA Student Member
†Professor, AIAA Associate Fellow

it. The same combustor is also operated in the premixed mode by simply shutting off the fuel supply (1) flowing through the central tube, and by discharging the fuel-air mixture through the annular tube into the combustor.

Several experimental investigations[4,5,6,7] have been carried to understand the flow features as well as the combustion characteristics in the SPRF combustor. Past studies have demonstrated the versatility of the combustor and its ease to operate stably with ultra-low emissions, low pressure losses, and appreciable power density in premixed, non-premixed and liquid fuel operation modes. These studies[4,5,6] used Particle Image Velocimetry (PIV), OH Planar Laser-Induced Fluorescence (PLIF) and chemiluminescence (heat release) measurements. Bobba *et al*[4,6] showed that flame was anchored in a region of low velocity and high turbulent intensities in the premixed mode. This resulted in a stable operation of the combustor even for very lean equivalence ratio without the need of external preheating or swirl. The measurements also showed large vortical structures entraining hot combustion products back into the reactant stream. This is found to increase the flammability of the lean mixtures, and also lower NO_x emissions due to the recirculation of the hot products. Most of the heat release was found to occur in the downstream portion of the combustor and also a thin-flame like structure was observed.

In addition to the experimental studies, numerical studies were also performed on the SPRF combustor. One such study by Sankaran *et al*[8] analyzed the salient features of the SPRF combustor using Large Eddy Simulations (LES). Both the reacting flow and non-reacting flow in the premixed case were investigated. However, the authors concluded that further improvement of the predictions was necessary. Another combined experimental and numerical study demonstrated by Gopalakrishnan *et al*[9] analyzed the effects of confinement, flow reversal and combustion of the flow field in the SPRF combustor. A simple eddy break up (EBU) model[10] was used to simulate the combustion-turbulence interactions. The simulated mean and RMS results showed qualitative agreement with the experiments.

In the current work, LES approach is used to study the premixed combustion mode in SPRF combustor. An advanced sub-grid combustion model known as Linear Eddy Mixing (LEM) model is used as a closure of the scalar mixing and the combustion. (This combined approach will be referred to as LEMLES, hereafter.) LEM had been successfully applied to scalar mixing,[11,12] premixed combustion,[13,14,15] non-premixed combustion[16,17] and pollutant emission.[15] These studies showed that LEMLES approach has the potential to address scalar mixing and combustion under a wide range of conditions.

This paper is organized as follows: The following section describes the LES formulation along with a summary of the sub-grid model used in this study. Section III provides the problem setup, which includes the details of the numerical method and boundary conditions. This section also discusses the validity of LES and LEM grid resolutions. The fourth section describes the results of the current simulations and finally conclusions are provided in section V.

II. Governing Equations

The governing equation of motion for an unsteady, compressible, reacting flow is employed in this study. The flow variables are decomposed into the resolved and unresolved (sub-grid) components by using a spacial filtering operation such as $f = \tilde{f} + f''$, where tilde $\tilde{}$ denotes resolved scale and double prime $''$ denotes unresolved sub-grid scale quantities. The $\tilde{f}$ is the Favre filtered variable and is defined as $\tilde{f} = \frac{\overline{\rho f}}{\bar{\rho}}$, where the overbar represents the spatial filtering.[18] Applying Favre filtering, the conservation equations of mass, momentum, and energy are modified into:

$$\frac{\partial \bar{\rho}}{\partial t} + \frac{\partial \bar{\rho}\tilde{u}_i}{\partial x_i} = 0 \tag{1}$$

$$\frac{\partial \bar{\rho}\tilde{u}_i}{\partial t} + \frac{\partial}{\partial x_j}[\bar{\rho}\tilde{u}_i\tilde{u}_j + \bar{p}\delta_{ij} - \bar{\tau}_{ij} + \tau_{ij}^{sgs}] = 0 \tag{2}$$

$$\frac{\partial \bar{\rho}\tilde{E}}{\partial t} + \frac{\partial}{\partial x_i}[(\bar{\rho}\tilde{E} + \bar{p})\tilde{u}_i + \bar{q}_i - \tilde{u}_j\bar{\tau}_{ji} + H_i^{sgs} + \sigma_i^{sgs}] = 0 \tag{3}$$

where all terms with superscript sgs denote sub-grid quantities that require closure. Also $\bar{\tau}_{ij}$ is the filtered viscous tensor, and $\bar{q}_i$ is the heat flux vector given by: $\bar{q}_i = -\bar{\kappa}\frac{\partial \tilde{T}}{\partial x_i} + \bar{\rho}\sum_{k=1}^{N_s}\tilde{h}_k\tilde{Y}_k\widetilde{V_{i,k}} + \sum_{k=1}^{N_s}q_{i,k}^{sgs}$. The filtered diffusion velocities are approximated using Fickian

diffusion as $\widetilde{V_{i,k}} = (-\bar{D}_k/\tilde{Y}_k)(\partial\tilde{Y}_k/\partial x_i)$. In the LEMLES approach, the species transport equations are solved without filtering (to be discussed later). As a result, the sub-grid term $q_{i,k}^{sgs}$ does not need closure in this approach. The other sub-grid terms that require closure are:

$$\begin{aligned} \tau_{ij}^{sgs} &= \overline{\rho}\ (\widetilde{u_i u_j} - \widetilde{u}_i\widetilde{u}_j) \\ H_i^{sgs} &= \overline{\rho}\ (\widetilde{Eu_i} - \widetilde{E}\widetilde{u}_i) + (\overline{pu_i} - \overline{p}\widetilde{u}_i) \\ \sigma_i^{sgs} &= \widetilde{u_j\tau_{ij}} - \widetilde{u}_j\overline{\tau}_{ij}. \end{aligned} \tag{4}$$

The pressure is determined from the filtered equation of state, $\bar{p} = \bar{\rho}R\tilde{T} + T^{sgs}$. Here, T^{sgs} is the temperature-species correlation term, defined as $([\widetilde{Y_k T} - \tilde{Y}_k\tilde{T}])/W_m$. This sub-grid term also does not need closure in LEMLES for the reason mentioned above. The filtered total energy per unit volume is given by $\bar{\rho}\tilde{E} = \bar{\rho}\tilde{e} + \frac{1}{2}\bar{\rho}\tilde{u}_i\tilde{u}_i + \bar{\rho}k^{sgs}$ where, the sub-grid kinetic energy (to be discussed later) is defined as, $k^{sgs} = (1/2)[\widetilde{u_k u_k} - \tilde{u}_k\tilde{u}_k]$. The filtered internal energy for calorically perfect gases is given by $\tilde{e} = \sum_{k=1}^{N_s}[c_{v,k}\tilde{Y}_k\tilde{T} + \tilde{Y}_k\Delta h_{f,k}^{'}]$ where, $\Delta h_{f,k}^{'} = \Delta h_{f,k}^0 - c_{p,k}T^0$ and $\Delta h_{f,k}^0$ is the standard heat of formation at a reference temperature T^0.

A. SGS Closure for LES equations

The sub-grid stress tensor τ_{ij}^{sgs} is modeled as $\tau_{ij}^{sgs} = -2\rho\nu_t[\tilde{S_{ij}} - \frac{1}{3}\tilde{S_{kk}}\delta_{ij}] + \frac{2}{3}\bar{\rho}k^{sgs}\delta_{ij}$. To complete the closure for the sub-grid stresses, the sub-grid eddy viscosity ν_t and the sub-grid kinetic energy, k^{sgs} need to be modeled. A non-equilibrium model[19,20] using a transport equation for the sub-grid kinetic energy, k^{sgs} is used in this study, and is given by :

$$\frac{\partial\overline{\rho}k^{sgs}}{\partial t} + \frac{\partial}{\partial x_i}\left(\overline{\rho}\tilde{u}_i k^{sgs}\right) = \frac{\partial}{\partial x_i}\left(\overline{\rho}\frac{\nu_t}{\sigma_k}\frac{\partial k^{sgs}}{\partial x_i}\right) + P^{sgs} - \epsilon^{sgs} \tag{5}$$

The terms, P^{sgs} and ϵ^{sgs} in the above equation are respectively, the production and the dissipation of sub-grid kinetic energy. The sub-grid dissipation, ϵ^{sgs} is obtained by integrating the dissipation spectrum ($D(k) = -2\nu k^2 E(k)$) over the unresolved wavenumbers, to get $\epsilon^{sgs} = C_\epsilon\rho(k^{sgs})^{3/2}/\overline{\Delta}$ where, $C_\epsilon = 0.916$.[21] The sub-grid production term is modeled as $P^{sgs} = -\tau_{ij}^{sgs}(\partial\widetilde{u}_i/\partial x_j)$. The coefficient σ_k is set to 0.9 for this study. The sub-grid eddy viscosity is modeled as $\nu_t = C_\nu\sqrt{k^{sgs}}\Delta$, where $C_\nu = 0.067$ nominally.[21] The current study aims to eliminate the use of these constants and hence we employ the dynamic procedure to evaluate the model coefficients. The dynamic procedure uses the assumption that there exists a scale similarity in the inertial sub-range turbulence. In other words, the largest unresolved sub-grid scales are statistically similar to the smallest resolved scales. The reader is referred to Kim and Menon[22] for a detailed discussion on the dynamic procedure.

In addition to τ_{ij}^{sgs}, the other unclosed terms that appear in the LES filtered equations are: H_i^{sgs}: sub-grid enthalpy flux; σ_i^{sgs}: sub-grid viscous work; The sub-grid total enthalpy flux H_i^{sgs} is modeled using the eddy viscosity model as follows: $H_i^{sgs} = (-\overline{\rho}\nu_t/Pr_t)(\partial\tilde{H}_k/\partial x_i)$. The other unclosed term, σ_i^{sgs} is often neglected in the conventional closure approach, and there exists no model.[23]

B. LEM closure for scalar transport

In LEMLES, the species transport equations are not filtered, instead the large scale advection, molecular diffusion, turbulent mixing by the action of eddies smaller than grid size, and chemical reaction are resolved at their respective time and length scales inside each LES cell. In order to describe this model mathematically, we split the velocity field as $u_i = \tilde{u}_i + (u_i')^R + (u_i')^s$. Here, $\tilde{u}_i$ is the LES resolved velocity field, $(u_i')^R$ is the LES resolved sub-grid fluctuation (obtained from k^{sgs}), and $(u_i')^s$ is the unresolved sub-grid fluctuation. Now, consider the unfiltered reactive scalar Φ using the above velocity split.

$$\rho\frac{\partial\Phi}{\partial t} = -\rho[\tilde{u}_i + (u_i')^R + (u_i')^s]\frac{\partial\Phi}{\partial x_i} - \frac{\partial}{\partial x_i}\left(\rho Y_k V_{i,k}\right)] + \dot{w}_\Phi \tag{6}$$

In LEMLES, the above equation is rewritten as

$$\frac{\Phi^* - \Phi^n}{\Delta t_{LES}} = -[\tilde{u}_i + (u_i')^R]\frac{\partial\Phi}{\partial x_i} \tag{7}$$

$$\Phi^{(n+1)} - \Phi^* = \int_t^{t+\Delta t_{LES}} -\frac{1}{\rho}\left[\rho(u_i')^s \frac{\partial \Phi^n}{\partial x_i} + \frac{\partial}{\partial x_i}(\rho \Phi V_{i,k})^n + \dot{w}_\Phi^n\right] dt' \tag{8}$$

Here Δt_{LES} is the LES time step. The large scale processes are governed by Eq. (7) and it represents the LES resolved convection of the scalar field. This equation is implemented in LEM using a Lagrangian transfer of mass across the finite volume surfaces. This transport is achieved using a "splicing" technique. Splicing involves the transfer of LEM cells between the LES control volumes accounting for the mass flux across each LES cell face. Further details are given elsewhere.[16,24,21] Equation (8) describes the small scale processes as viewed at the LES space and timescales. The right hand side of the Eq. 8 represents following three processes that occur within each LES grid: (1) sub-grid molecular diffusion, (2) chemical reaction, (3) sub-grid stirring. All these processes are modeled on a one-dimensional domain embedded inside each LES cell, where the integrand on the right hand side of the Eq. (8) is rewritten in terms of the sub-grid time and space scales. The one-dimensional domain in each LES cell is not physically oriented along any of the Cartesian (x,y,z) directions, but oriented in the direction of the local, instantaneous maximum scalar gradient.[25,26] The LEM one-dimensional domain is split into LEM cells, where the number of cells is chosen to ensure that all of the turbulent scales below the grid are resolved. As a result of this, all of the three processes represented in the Eq. (8) are closed in an exact manner. The sub-grid stirring term is implemented using stochastic rearrangement events called triplet maps.[25] This mapping is performed using the isotropy assumption for scalar fields, which is consistent with the LES approach. More details on the sub-grid processes are provided in a recent work by Menon.[27]

In LEM, combustion at the sub-grid level increases the temperature and decreases the local density. This is due to the assumption that sub-grid pressure is same as the resolved grid pressure. This assumption is valid as long as there are no strong pressure gradients. However, this effect results in a volumetric expansion and is included explicitly in LEMLES by expanding the LEM domain. The issues that arise due to this regridding are dealt in some other study.[27] Finally, the gist of the LEMLES can be stated as follows: In LEMLES, each of the processes namely molecular diffusion, chemical reaction, thermal expansion, sub-grid stirring and transport of sub-grid scalar field are implemented numerically as discrete events in time. The instants at which the processes occur depends on the respective time-scale of each of these processes.

III. Numerical Method and Boundary Conditions

The governing filtered unsteady compressible Navier-Stokes equations are discretized in time and space and solved using a finite-volume formulation in generalized co-ordinates. The numerical scheme is second-order accurate in space and time. The computational domain is resolved using a two-domain butterfly grid. A grid of $194 \times 75 \times 51$ is employed for the outer body-conforming grid and a grid of $194 \times 15 \times 15$ is employed in the central Cartesian grid. The grid is non-uniform and is clustered near regions of high gradients. The grid resolution is around $y^+ = 15$ near the walls of the injector. The axial grid is clustered around the point of jet expansion. It is then stretched after one jet diameter downstream and again near the stagnation end of the combustor. The grid stretching is less than 5% in the near field region, and stretching increases to a maximum of around 10% far away from the injector. With this resolution, nearly 15 points are in the outer shear layer width, which is considered adequate. Inflow and outflow boundary conditions are set using the characteristic conditions of Poinsot and Lele.[28] On all solid walls, no-slip conditions are prescribed for the velocity field. Adiabatic and non-catalytic wall boundary conditions are used for the temperature and the species field.

For the non-reacting case, a jet of air at atmospheric pressure and temperature flows into the combustor at a volumetric flow rate of $0.00638m^3/s$. The same flow rate is also maintained in the combustion case, but with a premixed mixture of methane-air with lean equivalence ratio of $\phi = 0.58$. (Accordingly, the velocity profile at the inflow is imposed in the LES study.) Using the mass flow rate, a peak velocity of $78m/s$ is used in the non-reactive case, while a peak value of $137m/s$ is used in the reactive case. The higher peaks in the reactive case is due to an effect observed in experiments. It was found that, as the incoming mixture flows through the injector, it is preheated to $500k$ ($1atm.$) before reaching

the tip of the injector. This is included in the computations by accelerating the inflow velocity at the injector tip to $137m/s$. Random turbulence with a RMS velocity profile with peak intensity of 15 % is superimposed on the mean velocity profile. In addition, a realistic profile of sub-grid kinetic energy is also imposed at the inflow. For the cold flow conditions, the Reynolds number based on the inlet bulk velocity and the annular injector width is 14.8×10^3, while the sub-grid Reynolds number based on the simulated k^{sgs} in the shear layer close to the injector is around 354.

In the non-reacting case, the comparison of LES results with PIV is performed by first running the simulations for one flow through time (to eliminate the transient effects) and then averaged for another two flow through times. The LEMLES simulations are also run for about a flow thorough time and then the instantaneous data is averaged for about another flow through time.

A four-step, seven-species reduced chemical mechanism, consisting of the two-step Westbrook and Dryer[29] methane-air mechanism and a two-step NO chemistry involving thermal and non-thermal NO formation[30] is used to find the chemical reaction rates. The reaction steps are as follows:

$$CH_4 + \frac{3}{2}[O_2 + 3.76N_2] \rightarrow CO + 2H_2O \quad (9)$$

$$CO + \frac{1}{2}O2 \rightarrow CO_2 \quad (10)$$

$$N_2 + O_2 \rightarrow 2NO \quad (11)$$

$$N_2 + O_2 \rightarrow 2NO \quad (12)$$

A. LES and LEM grid resolution

In LES, the grid is chosen to resolve the inertial range length scales. The validity of the grid resolution is assessed by studying the Fast Fourier Transform of the kinetic energy contained in the axial velocity component, $E_{1,1}$. This energy spectrum is shown in Fig. 2. In the plot, the region where the energy decays follows the Kolmogorov's -5/3 law for atleast one decade. This is considered to be well resolved and thus the computational grid used in this study is reasonable for LES.

The resolution of the LEM computational domain is determined by the LES-unresolved turbulence. Using scale relations and the simulated k^{sgs} values of the non-reactive jet, the Kolmogorov scale η is evaluated in regions of high turbulence and the smallest η is found to be around $0.06mm$. Based on this number, using 12 LEM cells in each LES cell is found to be appropriate. Each LEM cell is around $0.063mm$ and hence resolves upto η. Also calculations are performed using the CHEMKIN package and flame thickness is evaluated in the regions of interest. The ratio of flame thickness to Kolmogorov's scale is estimated to be around 30. In a typical lean premixed system, the reaction zone thickness is $1/10$ of the flame thickness.[23] Hence the simulations are able to resolve the reaction zone with 3 LEM cells. Furthermore, atleast 3 cells are needed to resolve the flame at LES level. This requirement is also met in the current studies.

IV. Results and Discussion

Results obtained from the large-eddy simulation of the stagnation point reverse flow (SPRF) combustor are presented here. The results section is divided into two sections. The first section presents the non-reactive flow in the premixed mode. The next section presents the reactive flow in the premixed mode using the LEM sub-grid closure.

A. Non-Reactive jet

The flow configuration is shown in Fig. 1. It consists of an annular jet of air flowing from the injector into the combustor. In the experiments, the central tube was shut-off far upstream to prevent any flow from the central tube. This creates a cylindrical cavity, into which the fluid from the combustor can flow in. To accurately simulate the flow conditions, this cylindrical cavity is also included in the computations. However, to reduce the computational cost, the length of the cylindrical cavity is restricted to be equal to the length of the injector.

Figure 3 shows the variation of the mean axial velocity along the center-line of the combustor. Overall, there is very good agreement between the time-averaged LES and PIV data. The plot shows that along the centerline, the annular jet is slowed down by the presence of cylindrical cavity. This causes a small recirculation bubble at the tip of the injector, near the center tube. As the fluid continues to flow, the shear layers merge and accelerates the flow to a peak velocity of $67m/s$. The axial velocity begins to decay rapidly as the flow approaches the stagnation end of the combustor and significant portion of the flow stagnates well upstream of the end wall. As a result, the classical stagnation point flow[31] is not seen at the end wall of the combustor. The experimental results are well predicted by the LES studies.

Figure 4 shows the mean axial velocity profiles at four axial locations in the combustor. The comparison of LES results with PIV data shows good agreement. The computations exhibit more symmetry than the measurements, and measured asymmetry is likely due to the slight misalignment of the inner tube within the annular injector. Near $x = 57$ and $113mm$ from the injector, both LES and PIV show high reverse flow velocity. This causes a rapid growth of the mixing layer in this region, which saturates after approximately half the length of the combustor. After this point, the flow around the center-line of the combustor feels presence of the stagnation region and slows down rapidly, resulting in a more uniform velocity profile near the stagnation end of the combustor.

Figure 5 shows the comparison of RMS axial velocity profiles at four axial locations in the combustor. Note that LES only shows the resolved part of the turbulence intensities. The agreement between PIV and LES are quite satisfactory near the injector and shows very little discrepancy downstream. Both LES and PIV show a spread of RMS levels near $X = 113mm$.

Figures 3, 4, and 5 show that the LES is able to resolve all the requisite scales and capture the relevant flow features with good accuracy. The rest of this paper deals with the application of LEMLES to understand the combustion characteristics in SPRF combustor.

B. Reactive jet

Figure 6 shows the comparison of average heat release zones in the computations and experiments. In the experiments, the heat release is obtained by averaging the chemiluminescence field, while in computations, the heat release is obtained by averaging the heat release corresponding to the most exothermic chemical reaction, 11. Although, the comparison is not perfect, the figure provides information about where the heat release occurs in experiments and computations. Experiments show that most of the heat release occurs downstream of the combustor. The chemiluminescence field does not appear near the injector, but Bobba *et al*[4] mentioned that the heat release occurs essentially up to the injector lip. This suggests a weakly attached flame. However LEMLES predict a strong attached flame. This is mainly attributed to absence of any heat loss models near the injector tip in the computations. The heat release in computations occurs uniformly throughout the shear layer and at the center of the combustor. Both computations and experiments agree on how far into the combustor the heat release occurs. However, the heat release in computations occurs in a more compact sense when compared to the experiments. This could be attributed to the heat losses that occur at the combustor outer walls in experiments (one quarter of the combustor is not insulated while performing the laser diagnostics[4]), while the computations are run with adiabatic walls.

Figures 7(a) and (b) show the contours of the mean axial velocity and RMS axial velocity, respectively. The mean field exhibits reverse flow velocities as high as $40m/s$ and indicates a thick shear layer. The thickness of the shear layer can be identified by the high RMS regions in Fig. 7(b). The presence of this thick shear layer in SPRF combustor suggests that jet spreads and that the products exiting in the reverse direction are most likely to mix with the incoming reactants. The fluctuating velocities remain high until two-third ($x = 200mm$) of the combustor length. This results in a region of low mean velocity but with high fluctuations. This region also corresponds to the region of high heat release.

The region of low mean flow and high turbulence intensities can be observed in the centerline variation of mean and RMS axial velocities. This variation of mean is given in Fig. 8 and the variation of RMS is shown in Fig. 9. At about $x = 225mm$, the mean centerline velocities are low and the turbulent intensities are high. This region is the primary stabilization zone in the SPRF combustor. Figure 8 shows that LEMLES captures quite well the centerline variation of the mean axial velocity. The velocity magnitudes are

slightly overpredicted throughout the regions of heat release, and underpredicted very near the injector and at the very end of the combustor. The overprediction is due to the strong heat release and gas expansion on the fluid flow.

Figure 10 compares the numerical and experimental radial profiles of mean axial velocity at four axial locations. The agreement between the PIV data and the LES is quite good. Again, the PIV data is asymmetric for reasons mentioned earlier. The prediction of the axial velocity strongly depends on the location of the heat release. The good agreement in Fig. 10 suggests that the LEMLES has predicted the heat release at the right locations. However, there is discrepancy in the strength of the heat release, as shown in Fig. 6. This discrepancy is clearly visible in the prediction of radial profiles of RMS axial velocity shown in Fig. 11.

In the SPRF combustor, there is no external preheating. The turbulent large scale motions in the shear layer contribute significantly to preheating of the fuel-air mixture by entraining the hot products. Thus, in SPRF geometry, there is internal exhaust recirculation. This is demonstrated in the computations. Figures 12(a) and (b) respectively, show the velocity vectors colored by product (H_2O) concentration. Entrainment of products is clearly evident in computations. Combustion products are entrained into the shear layer, thereby preheating the reactants. This can be visualized by a parameter defined as the ratio of the mass of the products to the mass of the reactants, f_p. The contours of f_p are shown in Fig. 13(a). A 0 value of f_p correspond to the region where there are no products and a value of 0.25 corresponds to region with the largest amount of products.

Depending on the amount of products entrained, different flame speeds can be obtained using the CHEMKIN package. Using the flame speed and the flame thickness, Karlovitz number (Ka) defined for LES[32] has been evaluated. A value of Ka less than 100 (but greater than 1) is considered to be in thin reaction zone regime.[32] In this regime, the flame is thick but the reaction zone is still thin. A value of Ka greater than 100 is considered to be a broken reaction zone, where the Kolmogorov size eddies are small enough to penetrate the inner layer of the flame and alter the laminar flame structure. In the SPRF combustor, for the range of f_p(refer Fig. 13(a)) found in the computations, Ka is found to be less than 100. This can be visualized in Fig. 13(b), which shows the isocontours of reaction rates colored by the Karlovitz number. The color blue in Fig. 13(b) denote the values of Ka less than 100 and the color red denote the values of Ka greater than 100. Clearly, all of the combustion occurs in the thin reaction zones with the exception of few isolated points in the broken reaction zone. However, it should be noted that the above Ka values are based on an average f_p value. Hence, few locations with different f_p values are chosen from the Fig. 13(a) and the values of Ka are evaluated. These locations are marked on the regime diagram of the turbulent premixed combustion[32] and shown in figure 13(c). All the locations fall in the thin flame zones.

Experiments[4] also demonstrated the location of the flame zone and the penetration of the reactants. This was done using the gradient information obtained from the OH PLIF data. In order to provide a comparison, the processed OH PLIF data is compared to the averaged reaction rates of the fuel break up reaction. The comparison is shown in Fig. 14. In both the experiments and computations, dark regions inside the flame represents pure reactants. Figure 14 shows that along the center-line, the location at which reactions begin to occur is accurately predicted by the computations. Also, the width of the reactants zone is also well predicted.

Emission measurements performed on SPRF combustor indicated that the NO_x levels around 1 ppm can be achieved in premixed mode of operation. The computations also predicted very low levels of NO_x emissions. Figure 15(a) shows the contours of the NO_x concentration. Typically NO_x follows the temperature distribution, the contours of which are shown in Fig. 15(b). However, NO_x can also be generated via non-thermal pathways. The current simulations included two steps for NO_x generation: one step is a global step for non-thermal path and the other step is a global step for thermal path. Hence, in the computations, a distinction can be made between the generation of NO_x due to thermal and non-thermal routes. These paths for NO production is shown in Figs. 16(a) and (b). The NO production through non-thermal path is significant only in the flame zone, whereas the NO production through the thermal path is significant in the regions of high temperatures. However, the magnitude of reaction rates are higher in the non-thermal reaction suggesting that NO_x emissions are limited by the NO produced in the heat release regions. These results are in good agreement with experimental observations.[4]

V. Conclusions

LES of a new type of combustor (SPRF) is carried over using s sub-grid mixing and combustion model to accurately capture the flame structure and its characteristics. The study demonstrated that, with the use of appropriate grid, LEMLES is able to capture all the requisite physics with good agreement with data. The presence of regions with low mean velocity and high turbulence intensities, recirculation product packets, and high heat release are all reasonably well predicted by LEMLES. Simulations show a strong attached flame in contrast to a weakly attached flame predicted by the experiments. Comparison shows that computations agree well with the location of the flame zone and the penetration of the reactants. The SPRF combustor performs with very low emissions. This is also demonstrated by the current simulations. Analysis shows that the SPRF combustor operates in the thin reaction zone regime.

Acknowledgments

This work is supported by the NASA's URETI (University Research, Engineering, Technology Institute) program.

References

[1]**Tsuji, H., Gupta, A., Hasegawa, T., Katsuki, M., Kishimoto, K., and Morita, M.,** ***High Temperature Air Combustion: From Energy Conservation to Pollution Reduction*****, CRC Press, 2003.**

[2]**Wunning, J. A. and Wunning, J. G., "Flameless oxidation to reduce thermal NO-formation,"** ***Progress in energy and combustion science*****, Vol. 29, 1997, pp. 81–94.**

[3]**Neumeier, Y., Zinn, B., Weksler, Y., Seitzman, J., Jagoda, J., and Kenny, J., "Novel Combustor for Ultra Low Emissions with Non Premixed Reactants Injection,"** ***AIAA-2005-3775, 41st AIAA Joint Propulsion Conference*****, 2005.**

[4]**Bobba, M., Gopalakrishnan, P., Seitzman, J., and Zinn, B., "Characteristics of combustion processes in a stagnation reverse flow combustor,"** ***GT2006-91217, Proceedings of GT2006, ASME Turbo Expo 2006*****, 2006.**

[5]**Gopalakrishnan, P., Bobba, M. K., and Seitzman, J. M., "Controlling Mechanisms for Low NOx Emissions in a Non-Premixed Stagnation Point Reverse Flwo Combustor,"** ***Proceedings of the Combustion Institute*****, Vol. 31, 2006.**

[6]**Bobba, M. K., Gopalakrishnan, P., Radhakrishnan, A., Seitzman, J. M., Neumeier, Y., Zinn, B. T., and Jagoda, J., "Flame Stabilization and Mixing Studies in a Novel Ultra-Low Emissions Combustor,"** ***AIAA-2006-963, 44th AIIA Aerospace Sciences Meeting and Exhibit*****, 2006.**

[7]**Crane, J., Neumeier, Y., Jagoda, J., Seitzman, J., and Zinn, B. T., "Stagnation-Point Reverse-Flow Combustor Performance with Liquid Fuel Injection,"** ***GT2006-91338, Proceedings of GT2006, ASME Turbo Expo 2006*****, 2006.**

[8]**Sankaran, V., Gopalakrishnan, P., Undapalli, S., Parisi, V., Seitzman, J., and Menon, S., "A LES - PIV investigation of a stagnation point reverse flow combustor,"** ***AIAA-2005-3969, 41st AIAA Joint Propulsion Conference*****, 2005.**

[9]**Gopalakrishnan, P., Undapalli, S., Bobba, M., Sankaran, V., Menon, S., Zinn, B. T., and Seitzman, J., "MEasurements and Modeling of the Flow Field in an Ultra-Low Emissions Combustor,"** ***AIAA-2006-962, 44th AIIA Aerospace Sciences Meeting and Exhibit*****, 2006.**

[10]**Fureby, C. and Lofstrom, C., "Large Eddy Simulation of Bluff Body Stabilized Flames,"** ***Proceedings of the Combustion Institute*****, Vol. 25, 1994, pp. 1257–1264.**

[11]**Chakravarthy, V. and Menon, S., "Large-Eddy Simulations of Reynolds and Schmidt Number Dependencies in Turbulent Scalar Mixing,"** ***Physics of Fluids*****, Vol. 13, 2001, pp. 488–499.**

[12]**Sankaran, V. and Menon, S., "LES of Scalar Mixing in Supersonic Shear Layers,"** ***Proceedings of the Combustion Institute*****, Vol. 30, 2004, pp. 2835–2842.**

[13]**Chakravarthy, V. and Menon, S., "Subgrid Modeling of Premixed Flames in the Flamelet Regime,"** ***Flow, Turbulence and Combustion*****, Vol. 65, 2000, pp. 133–161.**

[14]**Sankaran, V. and Menon, S., "Subgrid Combustion Modeling of 3-D Premixed Flames in the Thin-Reaction-Zone Regime,"** ***Proceedings of the Combustion Institute*****, Vol. 30, 2005, pp. 575–582.**

[15]**Eggenspieler, G. and Menon, S., "Combustion and Emission Modeling near Lean Blow-Out in a Gas Turbine Engine,"** ***Progress in Computational Fluid Dynamics*****, Vol. 5, 2005, pp. 281–297.**

[16]**Menon, S. and Calhoon, W., "Subgrid Mixing and Molecular Transport Modeling for Large-Eddy Simulations of Turbulent Reacting Flows,"** ***Proceedings of the Combustion Institute*****, Vol. 26, 1996, pp. 59–66.**

[17]**Calhoon, W. H., Menon, S., and Goldin, G., "Comparison of Reduced and Full Chemical Mechanisms for Nonpremixed Turbulent H2-Air Jet Flames,"** ***Combustion Science and Technology*****, Vol. 104, 1995, pp. 115–141.**

[18]**Erlebacher, G., Hussaini, M. Y., Speziale, C. G., and Zang, T. A., "Toward the Large-Eddy Simulation of Compressible Turbulent Flows,"** ***Journal of Fluid Mechanics*****, Vol. 238, 1992, pp. 155–185.**

[19]**Schumann, U., "Subgrid Scale Model for Finite Difference Simulations of turbulent Flows in**

Plane Channels and Annuli," *Journal of Computational Physics*, Vol. 18, 1975, pp. 376–404.
[20]Menon, S., Yeung, P.-K., and Kim, W.-W., "Effect of Subgrid Models on the Computed Interscale Energy Transfer in Isotropic Turbulence," *Computers and Fluids*, Vol. 25, No. 2, 1996, pp. 165–180.
[21]Chakravarthy, V. and Menon, S., "Large-Eddy Simulations of Turbulent Premixed Flames in the Flamelet Regime," *Combustion Science and Technology*, Vol. 162, 2001, pp. 175–222.
[22]Kim, W.-W., Menon, S., and Mongia, H. C., "Large Eddy Simulations of a Gas Turbine Combustor Flow," *Combustion Science and Technology*, Vol. 143, 1999, pp. 25–62.
[23]Poinsot, T. and Veynante, D., *Theoretical and Numerical Combustion*, Edwards, Inc., 2001.
[24]Smith, T. M. and Menon, S., "Subgrid Combustion Modeling for Premixed Turbulent Reacting Flows," *AIAA-98-0242*, 1998.
[25]Kerstein, A. R., "Linear-Eddy Model of Turbulent Transport II," *Combustion and Flame*, Vol. 75, 1989, pp. 397–413.
[26]Menon, S., McMurtry, P., and Kerstein, A. R., "A Linear Eddy Mixing Model for Large Eddy Simulation of Turbulent Combustion," *LES of Complex Engineering and Geophysical Flows*, edited by B. Galperin and S. Orszag, Cambridge University Press, 1993.
[27]Menon, S. and Patel, N., "Subgrid Modeling for Simulation of Spray Combustion in Large-Scale Combustors," *AIAA Journal*, Vol. 44, No. 4, 2006, pp. 709–723.
[28]Poinsot, T. and Lele, S., "Boundary Conditions for Direct Simulations of Compressible Viscous Flow," *Journal of Computational Physics*, Vol. 101, 1992, pp. 104–129.
[29]Westbrook, C. K. and Fredderick, L. D., "Simplified Reaction Mechanisms for the oxidation of hydrocarbon fuels in flames," *Combustion Science and Technology*, Vol. 27, 1981, pp. 31–43.
[30]Nicol, D. G., Malte, P. C., Hamer, A. J., Roby, R. J., and Steele, R. C., "Development of a Five-Step Global Methane Oxidation-NO Formation Mechanism for Lean-Premixed Gas Turbine Combustion," *Journal of Engineering for Gas Turbines and Power*, Vol. 121, 1999, pp. 272–280.
[31]Frank, M. W., *Viscous Fluid Flow*, McGraw-Hill International Editions, 1991.
[32]Pitsch, H. and Duchamp De Lageneste, L., "Large-Eddy Simulation of Premixed Turbulent Combustion using a Level-Set Approach," *Proceedings of the Combustion Institute*, Vol. 29, 2002, pp. 2001–2008.

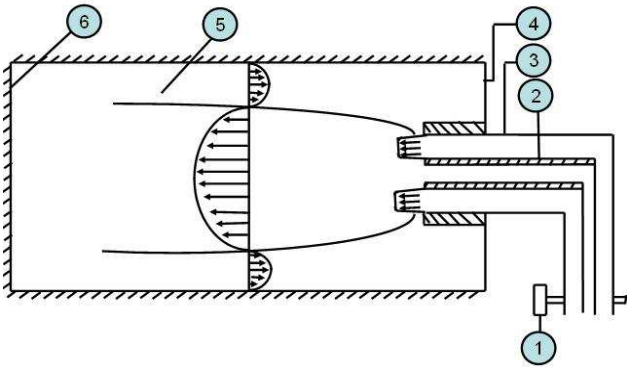

Figure 1. Schematic diagram of the Stagnation Point Reverse Flow Combustor

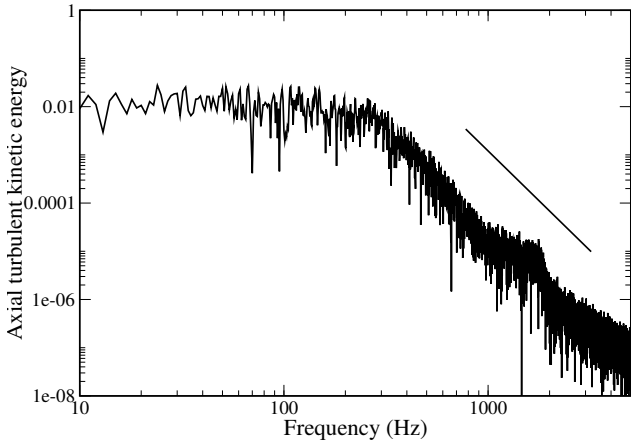

Figure 2. FFT of the axial turbulent kinetic energy for the non-reactive jet

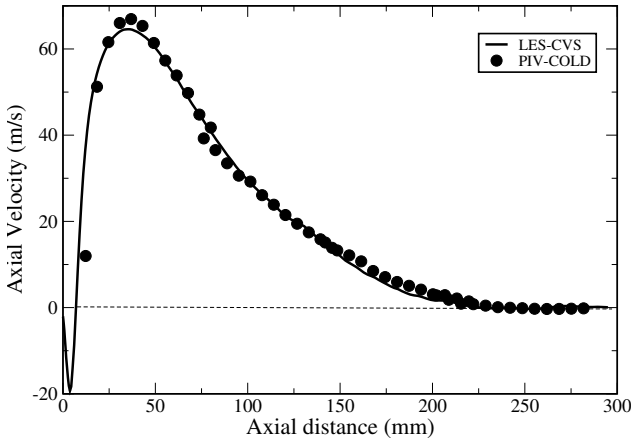

Figure 3. Comparison of Center-line mean axial velocity for the non-reactive jet

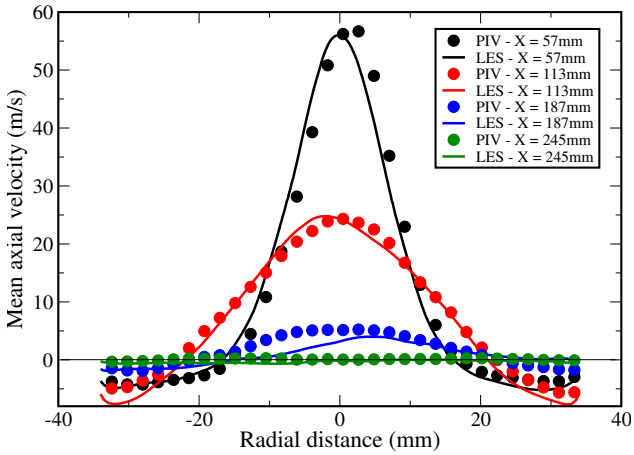

Figure 4. Comparison of radial profiles of mean axial velocity for the non-reactive jet

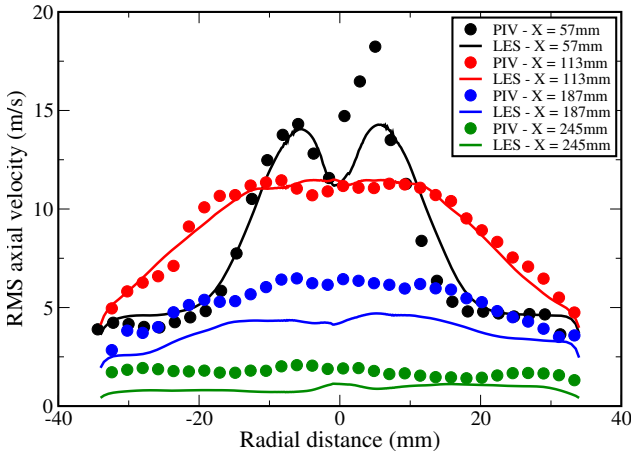

Figure 5. Comparison of radial profiles of RMS axial velocity for the non-reactive jet

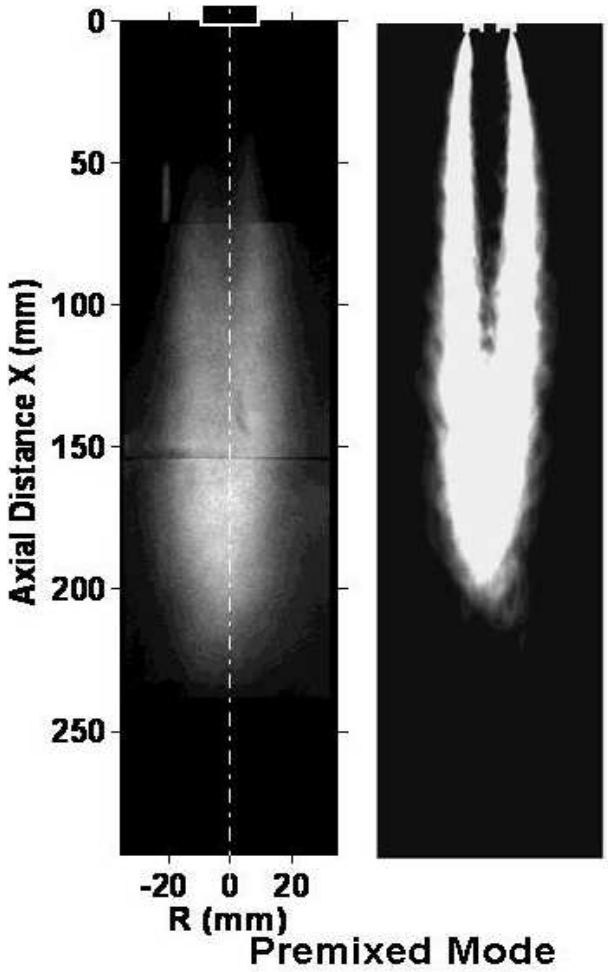

Figure 6. Comparison of averaged heat release in LES with averaged chemiluminescence field for the reactive jet

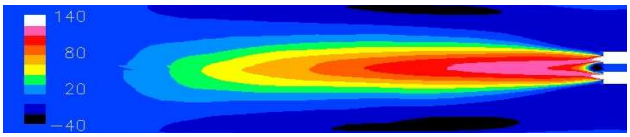

(a) Mean axial velocity contours

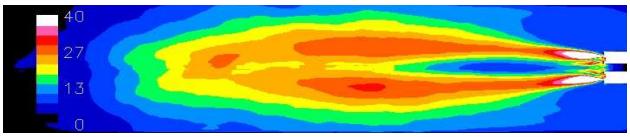

(b) RMS axial velocity contours

Figure 7. Contours of mean axial velocity and RMS axial velocity for the reactive jet

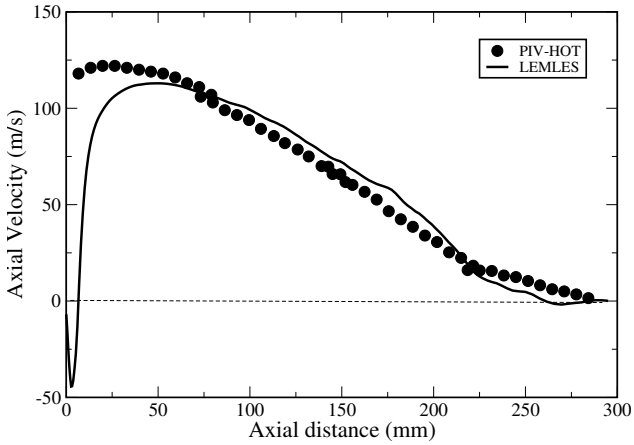

Figure 8. Comparison of Center-line mean axial velocity for the reactive jet

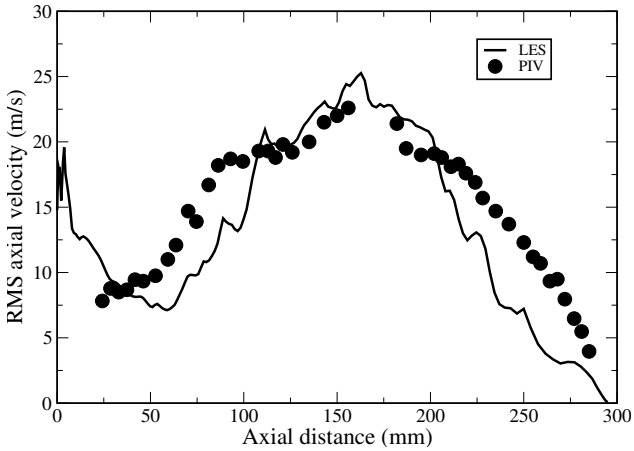

Figure 9. Comparison of Center-line RMS axial velocity for the reacive jet

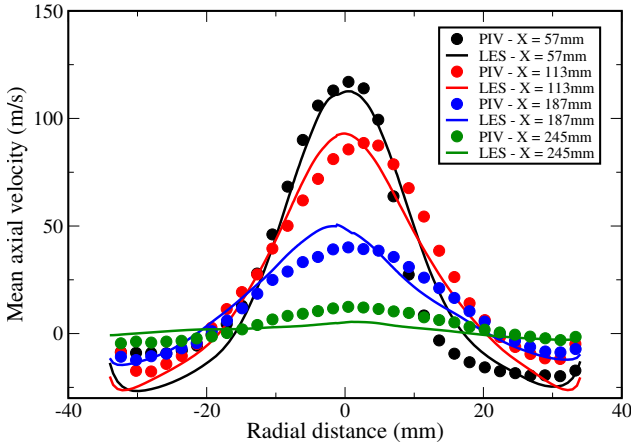

Figure 10. Comparison of radial profiles of mean axial velocity for the reactive jet

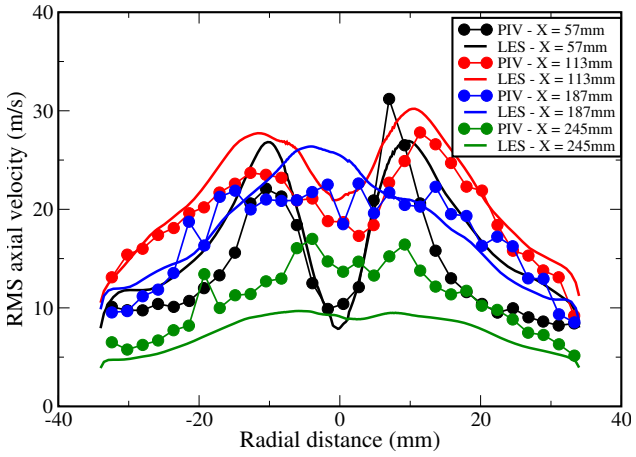

Figure 11. Comparison of radial profiles of RMS axial velocity for the reactive jet

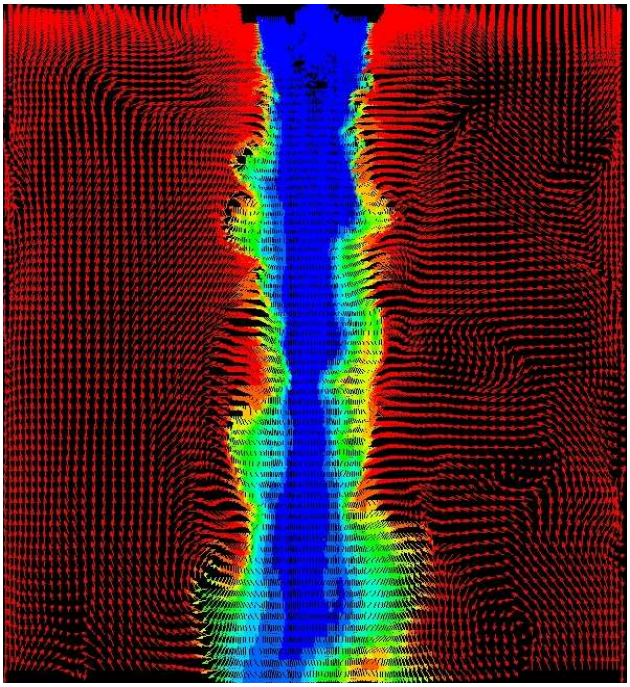

(a) First half of the combustor

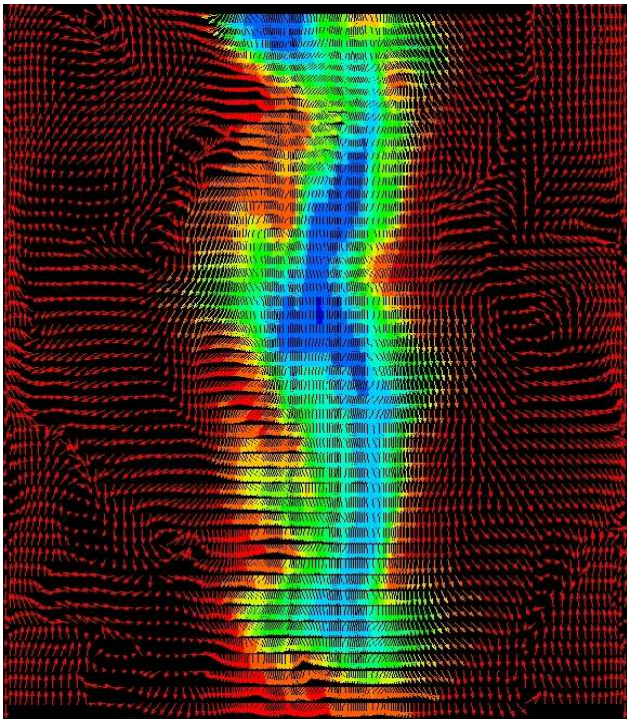

(b) Middle part of the combustor

Figure 12. Instantaneous velocity vectors colored by product (H_2O) concentration

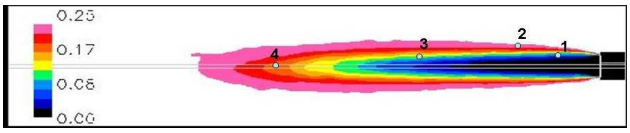

(a) Mean contours of the f_p defined as the amount of products to reactants. Points 1,2,3 and 4 denote locations with different f_p values

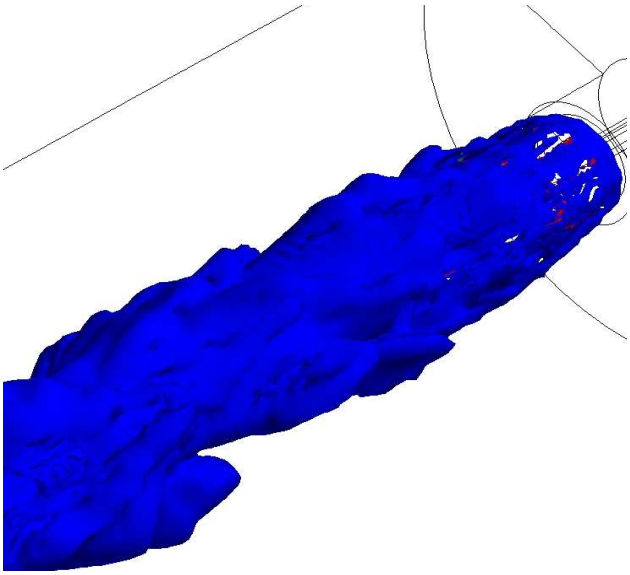

(b) Instantaneous isocontours of fuel destruction rate colored by Karlovitz number. Color blue indicates $Ka < 100$ and color red indicates $Ka > 100$

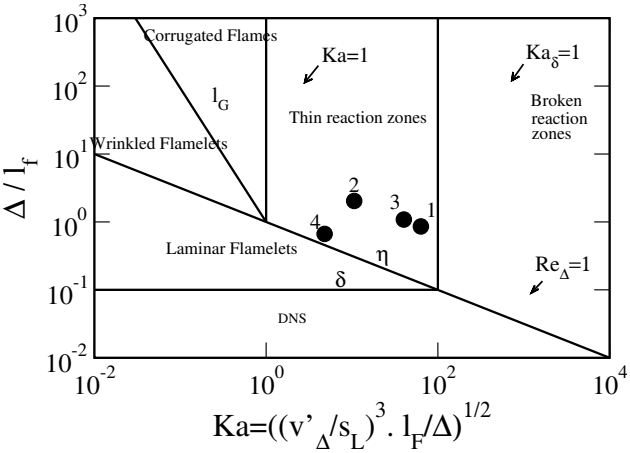

(c) Turbulent premixed combustion regime diagram. Points shown with different f_p values

Figure 13. Operating mode of SPRF combustor

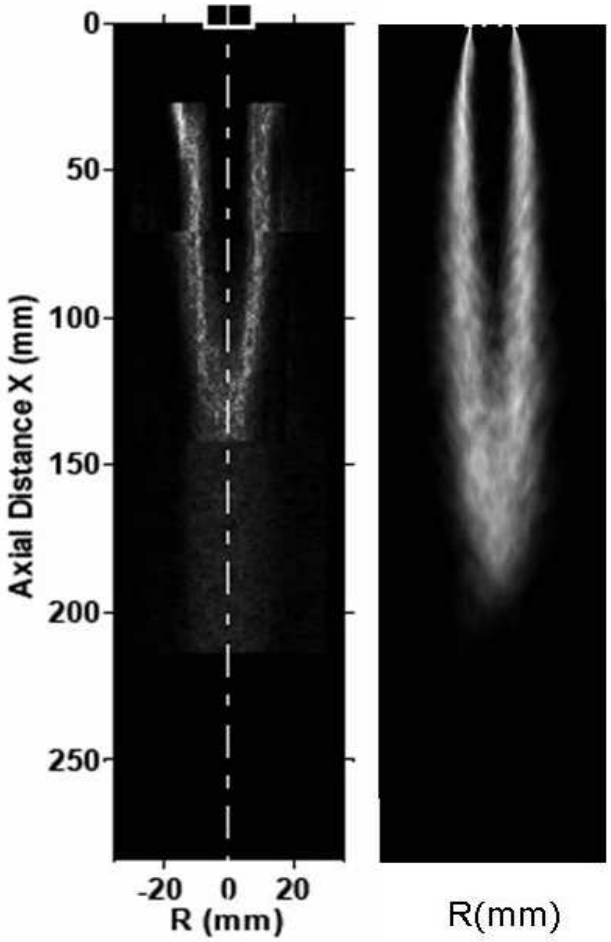

Figure 14. Comparison of flame location in computations and experiments

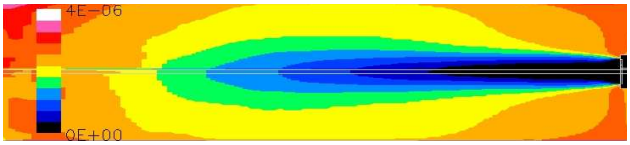

(a) Mean NO concentration contours

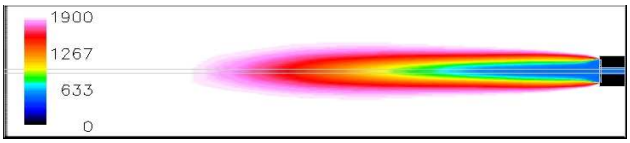

(b) Mean temperature contours

Figure 15. Contours of mean NO concentration and temperature

(a) Instantaneous contours of the non-thermal NO production rate

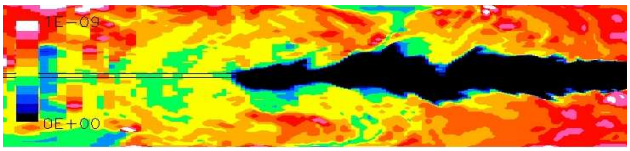

(b) Instantaneous contours of the thermal NO production rate

Figure 16. Instantaneous contours of NO production rate